

We are IntechOpen, the world's leading publisher of Open Access books Built by scientists, for scientists

6,900

Open access books available

185,000

International authors and editors

200M

Downloads

Our authors are among the

154

Countries delivered to

TOP 1%

most cited scientists

12.2%

Contributors from top 500 universities



WEB OF SCIENCE™

Selection of our books indexed in the Book Citation Index
in Web of Science™ Core Collection (BKCI)

Interested in publishing with us?
Contact book.department@intechopen.com

Numbers displayed above are based on latest data collected.
For more information visit www.intechopen.com



Optical Coherence Tomography for Polymer Film Evaluation

Jianing Yao and Jannick P. Rolland

Abstract

Development of functional polymer films and film stacks has been under increasing demand to create new generations of novel, compact, light-weight optics. Optical coherence tomography (OCT) is capable of evaluating all the important optical properties of a film or film stack, including topology of surfaces or layer-to-layer interfaces, the refractive index and thickness, and polarization property. By engineering the scanning architecture of an OCT system, high-precision metrology of films of either flat or spherical geometry is achieved. In this chapter, the system design, metrology methodologies, and examples of OCT for film metrology are discussed to provide both the knowledge foundation and the engineering perspectives. The advanced film metrology capabilities offered by OCT play a key role in the manufacturing process maturity of newly developed films. Rapid advancement in the field of OCT is foreseen to drive the application toward in-line film metrology and facilitate the rapid growth of innovative films in the industry.

Keywords: optical coherence tomography, optical metrology, nondestructive inspection, volumetric imaging, scanning architecture, films, surface topography, thickness metrology, refractive index metrology

1. Introduction

In recent years, the application of optical coherence tomography has expanded toward material characterization. The low-coherence nature of optical coherence tomography (OCT) leads to its niche in evaluating films ranging from several microns to a few millimeters thick. OCT is capable of evaluating all the important optical properties of a film or film stack, including topology of surfaces or layer-to-layer interfaces, the refractive index and thickness, and polarization property. OCT inspection of films bypasses the pitfalls of conventional laser Fizeau interferometry in testing film samples that have similar curvatures on both sides. The standard laser Fizeau interferometry is prone to spurious fringes due to the highly coherent light source; the artifacts are prominent when measuring a film sample where multi-reflections between top and bottom surfaces generate undesirable interferences that wash out the signal from the surface under test.

In this chapter, the OCT instrumentation tailored for film inspection is first introduced in Section 2. System calibration methods are described in Section 3 to ensure flat-field, distortion-free mapping of film samples. In Section 4, the methods for simultaneous metrology of the refractive index and thickness of films are

presented to inspire the readers. In Section 5, some examples are given to showcase the film metrology results achieved with OCT inspection.

2. Instrumentation

2.1 System architecture

OCT utilizes the interference of low-coherence broadband light, typically with wavelengths in the NIR region. Light divided by a beam splitter is sent to a sample arm that contains the sample under test and a reference arm with a reference mirror. Subsequently, back-reflected signals from the two arms are recombined to form interference fringes that are acquired by a detector for further analysis of the sample information. In time-domain OCT, interferometric fringes are generated by axially moving the reference mirror to match the optical path length of back-reflected signals at different depths of the sample. Interference is only observed when the optical path difference (OPD) between the reference and the sample is within the coherence length of the source.

In comparison, the advancement of Fourier-domain OCT (FD-OCT) has enabled high-speed and high-sensitivity depth-resolved three-dimensional (3-D) imaging of samples. FD-OCT utilizes the principle of light interference in the frequency domain, where reflected light from different depths inside a sample relative to the position of the reference reflector is encoded as different modulation frequencies on the detected spectrum at the interferometer exit. Therefore, no translation of the reference mirror is necessary to achieve depth-resolved imaging of a sample. With the increasing OPD between the reference reflector and the sample structure, spectral modulation frequency increases as well. The resulted summation of interference signals (an A-line spectrum, also referred to as a depth scan) contains spectral modulation frequencies contributed by sample structure at multiple depths. By performing a Fourier transform of the interference spectrum captured at the output of the interferometer, the sample reflectivity profile as a function of depth can be recovered, revealing the internal structure of the sample.

Synchronously with the acquisition of A-line spectra, lateral scanning can be performed either by scanning the focusing sample beam or laterally translating the sample itself. By combining the “depth scan” (no axial movement) and one-dimensional lateral scan, a cross-sectional image can be constructed. A 3-D data set can then be obtained by scanning in the orthogonal lateral dimension and combining the resulting, multiple cross-sectional images. The superb spectrally achieved depth discrimination capability of FD-OCT dramatically improves the imaging speed of OCT, allowing 3-D imaging of samples in real time.

Schematic layouts of an FD-OCT system are shown in **Figure 1**. The development of FD-OCT systems to date may be classified into two types as described in the figure. The first type is spectral domain OCT (SD-OCT) [1–3], in which the sample is illuminated by broadband light from a supercontinuum or superluminescent diode (SLD) source, and a spectrometer is used to collect the interference spectrum. The second type is the swept-source OCT (SS-OCT) [4–7], where a frequency-swept source is employed, in which instantaneous quasi-monochromatic light sweeps across a broad spectrum in a rapid cycle. Corresponding to the swept source, a single-element detector such as a photodiode is used to record the time-encoded spectral interference signal. Furthermore, the ability of FD-OCT to collect signals from the entire depth range of a sample during the entire acquisition time, sampled by multiple spectral channels, leads to significant signal-to-noise ratio (SNR) improvement of 20–30 dB over time-domain OCT

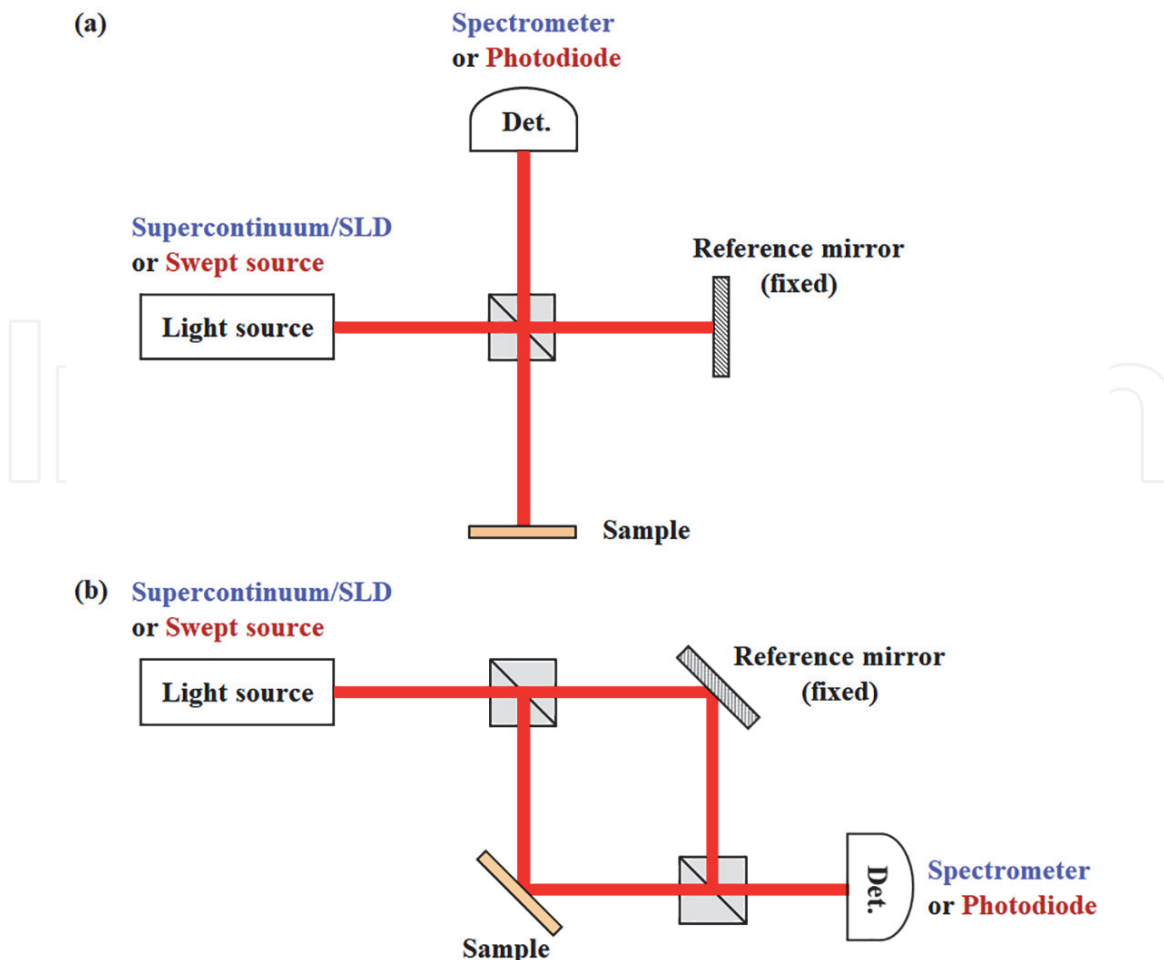


Figure 1. Schematic layout of typical configurations of an FD-OCT system: (a) Michelson configuration and (b) Mach-Zehnder configuration.

that employs a single-element detector to detect a restricted depth. State-of-the-art OCT systems built nowadays are predominantly FD-OCT.

Figure 1 shows two configurations of an FD-OCT system: (a) Michelson and (b) Mach-Zehnder configuration. It is well known that fringe visibility is maximized when the return power of the sample and reference arms are nearly matched. In the Michelson configuration, the portion of signal attenuation caused by double-pass through the beam splitter is identical for both the sample and reference beams; to generate the maximum amount of interference signal, the beam splitter needs to be at 50/50 split. On the other hand, in the Mach-Zehnder configuration, the power splitting ratio of the beam splitters can be carefully selected based on the optical property of the samples, such that the back-reflected signal of the reference beam balances with that of the sample beam. In this sense, the Mach-Zehnder configuration may allow achieving optimal signal-to-noise ratio at the detector. The ability to boost up sample beam relative to the reference beam is especially important for measuring multi-layer film samples where the back-reflection signals from inter-layer interfaces are weak.

2.2 System design considerations regarding axial point-spread-function and depth range

In OCT systems, the sample is illuminated by broadband light from a supercontinuum or SLD source. Key parameters to consider in designing an OCT system for film inspection are center wavelength, spectral bandwidth, and spectral

linewidth, which determine the axial point-spread-function (PSF) and depth range of an OCT system.

Assuming a Gaussian source spectrum, the full-width-at-half-maximum (FWHM) of the axial PSF of an OCT system, denoted as Δz , equals one-half the coherence length of the source as

$$\Delta z = \frac{2 \ln 2 \lambda_0^2}{\pi \Delta \lambda}. \quad (1)$$

where λ_0 is the center wavelength of the source spectrum and $\Delta \lambda$ is the FWHM of the wavelength spectrum.

It can be seen from Eq. (1) that the FWHM of the axial PSF is proportional to the square of the center wavelength of the light source, and inversely proportional to the bandwidth of the source spectrum. The FWHM of the axial PSF is a common figure of merit used to denote the capability of the system in terms of two-point resolution, which determines the minimal thickness of a film sample that an OCT system can resolve. However, the ability of the system to detect the variation in the axial position of a single reflector well exceeds the FWHM of the axial PSF; it is determined by the sensitivity of the system to sensing even nanometric axial displacements. This axial displacement sensitivity was empirically demonstrated to be often better than one part per thousand of the FWHM of the axial PSF.

It is also worth noting that the axial PSF can be significantly degraded by the dispersion mismatch between the reference and sample arms as a result of the dispersion characteristics of the fiber, sample, and optical components. Therefore, dispersion compensation approaches have been extensively developed by either hardware implementation [8, 9] or numeric correction [10–12].

Moreover, the axial PSF may also be altered by the optical properties of the imaging optics including transmittance, aberrations, polarization, and dispersion. For instance, chromatic aberration of the objective lens would alter the local effective bandwidth and degrade the axial PSF [13]. Therefore, achromatic, all-reflective optical designs may be beneficial for achieving the desired axial PSF of an OCT system.

Additionally, scanning noises, motion artifacts, and detection components may also perturb the axial PSF as well as the sensitivity of the system. All these factors need to be carefully taken into account during the system engineering of OCT instrumentation.

On the other hand, assuming sufficient depth of field provided by the imaging objective lens and an imaging depth range limited by the spectral linewidth that is assumed to be Gaussian in shape, the intrinsic single-sided imaging depth range of an OCT system, denoted as z'_{10dB} , is defined herein as the depth range leading to 10-dB sensitivity roll-off and is computed as

$$z'_{10dB} = \frac{0.895 \lambda_0^2}{\pi \delta_r \lambda}. \quad (2)$$

where $\delta_r \lambda$ is the FWHM of the Gaussian spectral line shape function.

It is worth noting that the sampling interval of the detector needs to be smaller than the instantaneous linewidth of the source in SS-OCT or the spectral resolution of the spectrometer in SD-OCT; otherwise, the usable imaging range will be limited by the sampling.

Finally, when designing an OCT system, a compromise between the axial PSF and imaging depth range usually needs to be considered. As has been shown, both the width of the axial PSF and the imaging depth range are proportional to the square of the center wavelength of the source λ_0^2 . Therefore, longer operating

wavelengths generally provide larger imaging depth range (although the absorption and scattering coefficients of a sample also need to be considered) at the expense of sacrificing the axial resolution; on the other hand, shifting to lower wavelength regime is expected to bring about better axial discrimination capability at the cost of faster sensitivity decay with depth. Moreover, once the operating wavelength λ_0 is fixed, to push for both a fine axial PSF and a large imaging depth, the challenge arises from the requirement of the system instrumentation to accommodate both a broad spectral bandwidth and a narrow spectral resolution. This would also mean high requirement on the high-speed frequency sweep of the source in SS-OCT, or the large array size of the CCD/CMOS camera in SD-OCT.

2.3 Lateral scanning approaches

FD-OCT enables superb depth sectioning of film samples. To form three-dimensional topography, a lateral scanning mechanism is employed, either by moving the OCT probe or translating the sample in a combination of two orthogonal directions. Different types of lateral scanning architectures are illustrated in **Figure 2**. To measure conventional film samples with flat surfaces, lateral scanning axes are set in Cartesian x and y directions as shown in **Figure 2a–e**; to perform in-situ measurements of curved film layers with spherical surfaces as a result of thermo-molding [14, 15], the lateral scanning axes may be constructed along the azimuthal and polar directions in a spherical coordinate system as shown in **Figure 2f**.

Among all the scanning configurations illustrated in **Figure 2**, **Figure 2e** and **f** move the sample platform by a pair of motorized stages orthogonal in either the Cartesian or spherical coordinates, depending on the curvature of the films under test. 2-D scanning of the sample platform is performed in a straightforward fashion. The straightness, orthogonality, and hysteresis characteristics of the stages are critical to the accuracy of the 3-D data collected. The stages are mechanically tuned to an optimal condition balancing the travel speed, range, and load. Displacement-measuring interferometers are often implemented to provide accurate, real-time feedback of the position of the motorized stages.

Alternative to scanning the sample platform, the beam that is incident on the sample may be sequentially deviated over a sampling grid by changing the angles of the scanning mirrors that are usually located on the path of the beam in the collimated space. Mirror-based scanning of sample beams has gained increasing popularity in OCT systems owing to the high scanning speed it has brought about. Scanning speed up to 500 Hz has been reported due to the low inertia of small mirrors, meaning an entire cross-sectional frame of data may be collected in 2 ms. Popular types of scanning mirrors are galvanometer-based or micro-electro-mechanical (MEMS) type. The common scanning configurations utilizing scanning mirrors in the sample arm of an OCT system are shown in **Figure 2a–c**. As denoted in the diagrams, a collimated beam is reasonably assumed to be the input to the sample arm. In a fiber-based OCT system, the collimated incoming sample beam is commonly formed by a collimating lens placed at one exiting port of a beam-splitting fiber-coupler. In a free-space OCT system, the output from a cube beam splitter dividing the sample and reference beams is collimated. For the simplicity of the illustration, any optics placed before the collimated beam input is omitted in the diagrams. In **Figure 2c**, a single 2-D MEMS scanning mirror may cover scanning field in the entire 2-D plane. In **Figure 2a** and **b**, 2-D scans are achieved by integrating two orthogonal 1-D scans in the x and y directions, respectively.

When scanning the sample beam, preserving telecentric scanning on a sample is crucial to distortion-free mapping of its surface profiles and internal structure, which requires the mirrors scanning in the x and y directions to collocate at the

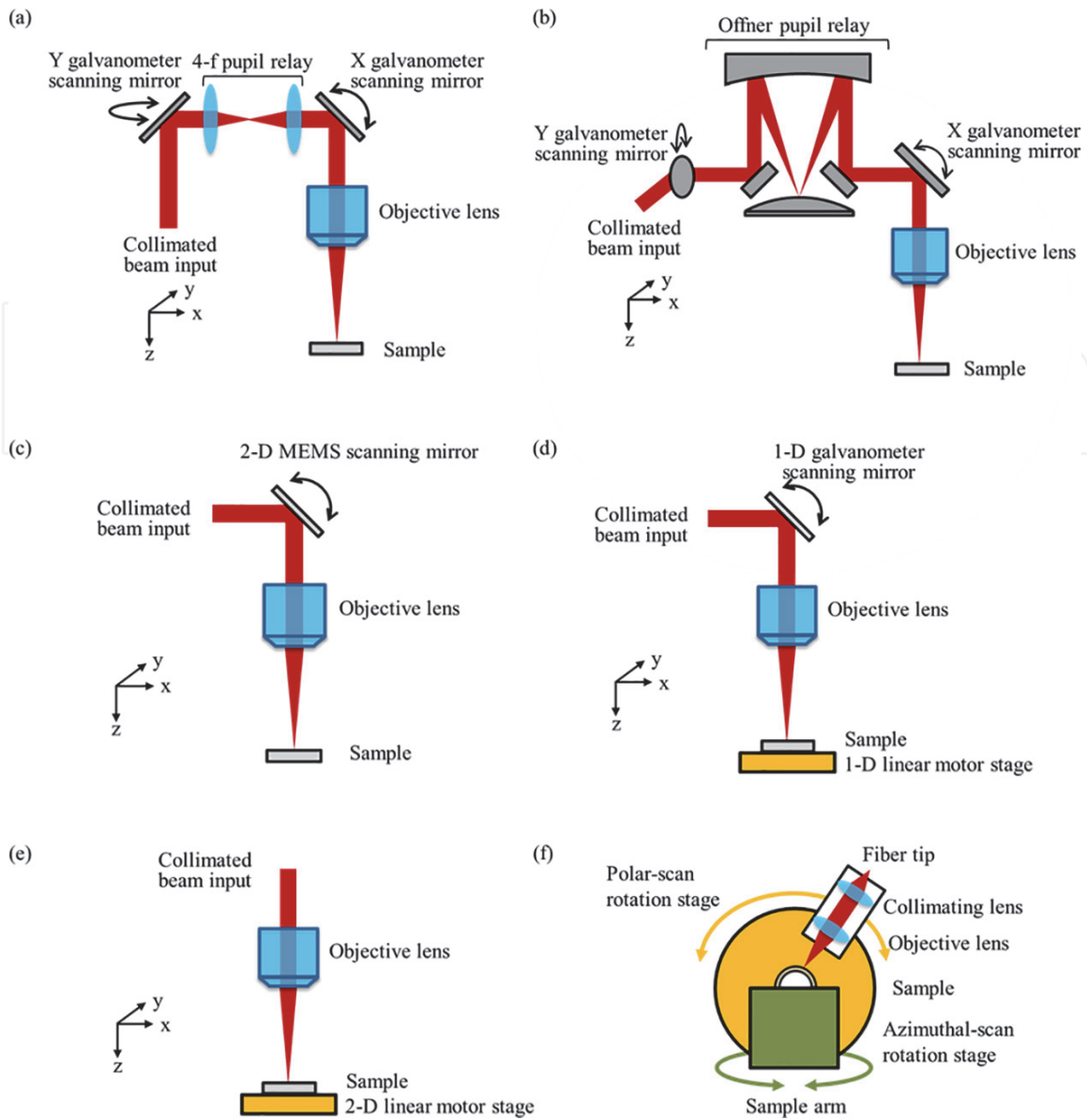


Figure 2. Illustration of the various lateral scanning configurations in the sample arm of OCT systems.

pupil plane (i.e., focal plane) of the objective lens. Such a scanning geometry is usually not supported by off-the-shelf dual-galvanometer-mirror systems where the pupil plane is simply compromised to be in between the two mirrors that are packaged in a small form factor. While this configuration with the aid of ray-tracing-based software calibration [16, 17] may be suitable for OCT systems toward biomedical imaging applications, it should be avoided in film metrology systems. Any displacement of the pivot of either or both the x - y scanning mirrors from the focal plane of the objective lens would inevitably lead to the deviation of the ray fan from being parallel to the optical axis, and thus introduce optical aberrations including astigmatism, field curvature, and distortion. To ensure the pivot point of both x and y scanning mirrors is at the pupil plane of the objective lens, three viable configurations are shown in **Figure 2a**, **b**, and **d**. **Figure 2d** provides a simple way to bypass the abovementioned pitfall by utilizing a combination of a single axis galvanometer beam steering along the fast-scan axis and a motorized linear stage translating along the orthogonal slow-scan axis. **Figure 2a** and **b** both create another optical conjugate of the pupil plane of the objective lens by implementing a pupil relay optical design. **Figure 2a** employs a refractive 4-f pupil relay design which often consists of a pair of achromatic doublets. **Figure 2b** shows an all-reflective

Offner pupil relay configuration with a concave primary, a convex secondary, and a pair of fold mirrors. The Offner relay carries the benefit of being free from chromatic aberrations across the broad spectral band of an OCT system and provides packaging advantage given its folded geometry.

3. Calibration

To obtain accurate quantitative results from OCT imaging, rigorous calibration of the system needs to be carried out, which generally requires vertical displacement calibration, discussed in Sections 3.1 to 3.3, and lateral scanning calibration, discussed in Section 3.4.

3.1 Spectral nonlinearity calibration

In SD-OCT, raw spectra collected by the CCD or CMOS array of the spectrometer are pseudo linear with the wavelength rather than with the frequency. Similarly, in SS-OCT, the frequency sweep generally is nonlinear with the frequency. In both cases, the detected spectra require calibration to the linear frequency space prior to Fourier transform that converts each spectral signal to a depth profile. The calibration can be achieved either in hardware or software.

In SS-OCT, hardware calibration is performed by using the time-frequency relation measured by an additional side MZI with a fixed optical path difference between its reference and sample arms as denoted by the dashed blue box in **Figure 3**. Simultaneous with the detection of the main interference signal, the calibration signal is detected by a second balanced photo-detector and then digitized by a high-resolution high-speed analog-to-digital converter. The locations of the peaks and valleys of the spectral interference signal from the side MZI that are physically linear in the frequency space provide the resampling scheme needed to recalibrate the spectral interference signal of the main OCT interferometer to be linear in the frequency space. The Fourier transform of a single recalibrated interference spectrum is then performed such that the result shows an entire component reflectivity profile as a function of the linear axial locations along the sample beam path.

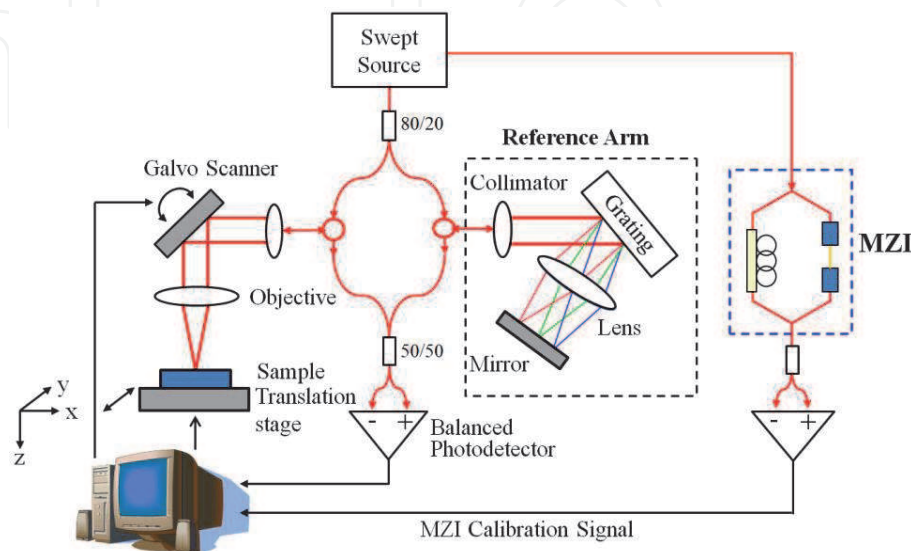


Figure 3. Layout of an SS-OCT system with a side MZI (denoted in dashed blue box) for spectral nonlinearity calibration.

3.2 Depth scale calibration

After the spectral nonlinearity calibration, rigorous calibration is required to accurately quantify the depth scale on a Fourier-transformed depth profile. Depth scale calibration can be achieved via various methods. A common approach is to image a series of different step height standards that cover the entire z -axis range of interest of the instrument. The details of this calibration approach are described elsewhere [18]. In this section, we describe an alternative method for depth scale calibration.

As show in **Figure 4**, a high surface quality flat mirror is placed in the sample arm where a high-precision motorized linear stage is set up to translate the mirror accurately along the z -axis. A high-resolution displacement measuring interferometer may be implemented to provide accurate feedback of the location of the motorized stage. For the depth scale calibration experiment, the motorized linear stage is controlled to move to a range of z locations covering the entire range of interest along the z -axis. A set of repeated measurements of interference spectra is acquired at each location. Through spectral nonlinearity calibration and subsequent Fourier transforms, depth profiles with a peak showing the mirror signal are restored. The relationship between the physical z positions of the mirror and the average pixel number of the mirror signal detected on the depth profiles are plotted in **Figure 4**. The inverse of the slope of the least squares fit line of the curve represents the depth scale.

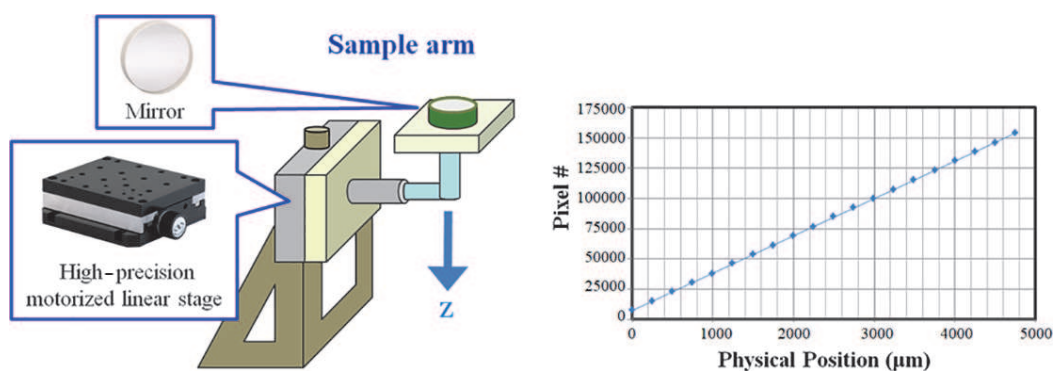


Figure 4. Illustration of depth scale calibration in OCT systems.

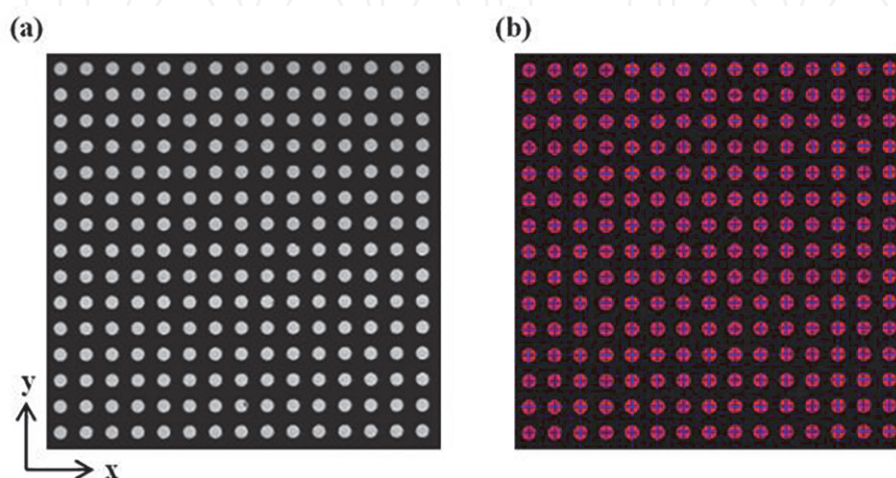


Figure 5. (a) A raw gray-scale x - y plane image of a dot grid target acquired by an SS-OCT under calibration. (b) a corresponding image after applying a centroiding algorithm to image (a), which shows the detected centroids (blue crosshairs) of the dots overlaying the dot grid (shown as enhanced red dots).

3.3 Field flatness audit

To form accurate 3-D volumetric data, it is important to eliminate any vertical displacement error that may be induced in 2-D scanning of the sample beam. For instance, field curvature may be induced by inaccurate positioning of the x and y scanning mirrors offset from the pupil plane of the objective lens. To inspect the flatness of the x - y scanning field, a high surface quality (e.g., $\lambda/20$) flat mirror may be imaged. Alternatively, a high-grade calibration ball standard may be imaged by angular-scanning OCT system to audit the alignment of the polar scanning axes. These calibration standards are easily measurable on laser Fizeau interferometers to verify the accuracy of the standards and compare against OCT measurement results.

3.4 Lateral scanning field audit and calibration

As described in Section 2.3, various lateral scanning mechanisms are employed in OCT systems to achieve 3-D volumetric imaging. To mitigate scan-induced

Evaluation Criterion	Formula
Linearity	
Physical dot locations (x, y) vs. pixel coordinates (P_x, P_y)	$\overline{P}_x(x) = \langle f_x(x, y) \rangle_y, \quad (3)$
	$\overline{P}_y(y) = \langle f_y(x, y) \rangle_x. \quad (4)$
Orthogonality	
Angle between x and y translation axes with an angle of θ_x and θ_y , respectively, from the horizontal direction of the dot array	$\theta_x = \left\langle \tan^{-1} \left[\frac{\sum_{m=1}^M (Mf'_x(m \cdot dx, y) - \sum_{m=1}^M f_x(m \cdot dx, y)) (Mf'_y(m \cdot dx, y) - \sum_{m=1}^M f_y(m \cdot dx, y))}{\sum_{m=1}^M (Mf'_x(m \cdot dx, y) - \sum_{m=1}^M f_x(m \cdot dx, y))^2} \right] \right\rangle_y, \quad (5)$
	$\theta_y = \left\langle \tan^{-1} \left[\frac{\sum_{n=1}^N (Nf'_x(x, n \cdot dy) - \sum_{n=1}^N f_x(x, n \cdot dy)) (Nf'_y(x, n \cdot dy) - \sum_{n=1}^N f_y(x, n \cdot dy))}{\sum_{n=1}^N (Nf'_x(x, n \cdot dy) - \sum_{n=1}^N f_x(x, n \cdot dy))^2} \right] \right\rangle_x. \quad (6)$
Straightness	
Deviation in the perpendicular direction from a true line of travel, residual error of $\varepsilon_x(x)$ for x -travel and $\varepsilon_y(y)$ for y -travel	$\varepsilon_x(x) = \langle f_y(x, y) \cos \theta_x - x \sin \theta_x - \cos \theta_x \frac{\sum_{m=1}^M f_y(m \cdot dx, y)}{M} + \sin \theta_x \frac{\sum_{m=1}^M f_x(m \cdot dx, y)}{M} \rangle_y, \quad (7)$
	$\varepsilon_y(y) = \langle f_x(x, y) \sin \theta_y - y \cos \theta_y - \sin \theta_y \frac{\sum_{n=1}^N f_x(x, n \cdot dy)}{N} + \cos \theta_y \frac{\sum_{n=1}^N f_y(x, n \cdot dy)}{N} \rangle_x. \quad (8)$
Sampling resolution	
Compute x and y pixel size $dP_x(x)$ and $dP_y(y)$ across the travel range	$dP_x(x) = \left\langle \frac{dx \cos \theta_x}{f_x(x + dx, y) - f_x(x, y)} \right\rangle_y, \quad (9)$
	$dP_y(y) = \left\langle \frac{dy \sin \theta_y}{f_y(x, y + dy) - f_y(x, y)} \right\rangle_x. \quad (10)$

Table 1. List of criteria and formulas used to evaluate the lateral scanning field from imaging a grid target (adapted from [19]).

lateral coordinate errors, the scanning field needs to be calibrated and periodically audited. The typical standards used for this purpose are dot grid targets. The size of the target covers the entire lateral field-of-view (FOV) of the OCT system.

Figure 5a shows an example of a raw gray-scale x - y plane image of a dot grid target acquired by an SS-OCT system with 2-D x - y stages for lateral scanning [19]. From the imaging, a centroiding algorithm is applied to locate the centers of the dots as shown in **Figure 5b**, where the dot grid enhanced in red is overlaid with the detected centroids in blue crosshairs. The two 2-D matrices storing the respective estimated horizontal and vertical pixel coordinates of the detected grid of centroids consist of M (column) \times N (row) elements, where M and N are the numbers of columns and rows of dots imaged, respectively.

Denoting the column and row indices of a dot as (m, n) , the nominal physical centroid location of the dot is described as $x = m \cdot dx$ and $y = n \cdot dy$, assuming dx and dy are constants representing the nominal horizontal and vertical separation between neighboring dots. On the other hand, the measured centroid location from the OCT image can be expressed in pixel coordinates as (P_x, P_y) . The mapping from (x, y) to (P_x, P_y) reflects the lateral scanning characteristics of the system and is expressed as $P_x = f_x(x, y)$ and $P_y = f_y(x, y)$. By analyzing the functions f_x and f_y , the attributes of the lateral scanning field consisting of linearity, orthogonality, straightness, and the sampling resolution are estimated as listed in **Table 1**. In the formulas, the notation of angle bracket $\langle \rangle$ with a subscript x or y denotes averaging over the horizontal or vertical direction of the dot array, respectively, to evaluate the mean (i.e., accuracy) and standard deviation (i.e., repeatability). From the metrics being evaluated from a dot grid target, calibration can be applied to correct the non-orthogonality of the two scanning axes or calibrate the distortion of the field.

4. Methodology for film thickness and refractive index metrology with OCT

To determine the refractive index of a sample, interferometric metrology techniques are generally confronted with the challenge that the measurand obtained reflects the optical thickness of a sample, which is a product of the refractive index and the physical thickness. Using low-coherence interferometry, several techniques have been proposed to decouple the index and physical thickness, which may be categorized into two main methodologies [20]: 1) evaluating the optical distortion of a reference induced by the sample inserted in the path [21–23] and 2) combining low-coherence interferometry with a focus tracking modality such as confocal scanning or multi-photon microscopy [24–27] to obtain another independent relation between index and thickness.

4.1 Simultaneous film thickness and refractive index metrology by evaluating optical distortion induced by a film sample in the sample path

The first method is based on evaluating the optical path length change induced by a film sample inserted in the path. This method is well suited for estimating the refractive index and thickness of a single-layer film using two types of measurements with the same OCT system. It does not require instrumentation modification and is readily adaptable to almost any OCT systems.

Figure 6a and **b** show a schematic cross-sectional view of the experimental setup in the sample arm. In the first step as shown in **Figure 6a**, the film under test is placed above a high-quality reference flat, with a small air gap in between, which is created by a thin ring spacer that supports the film sample in the periphery. Both

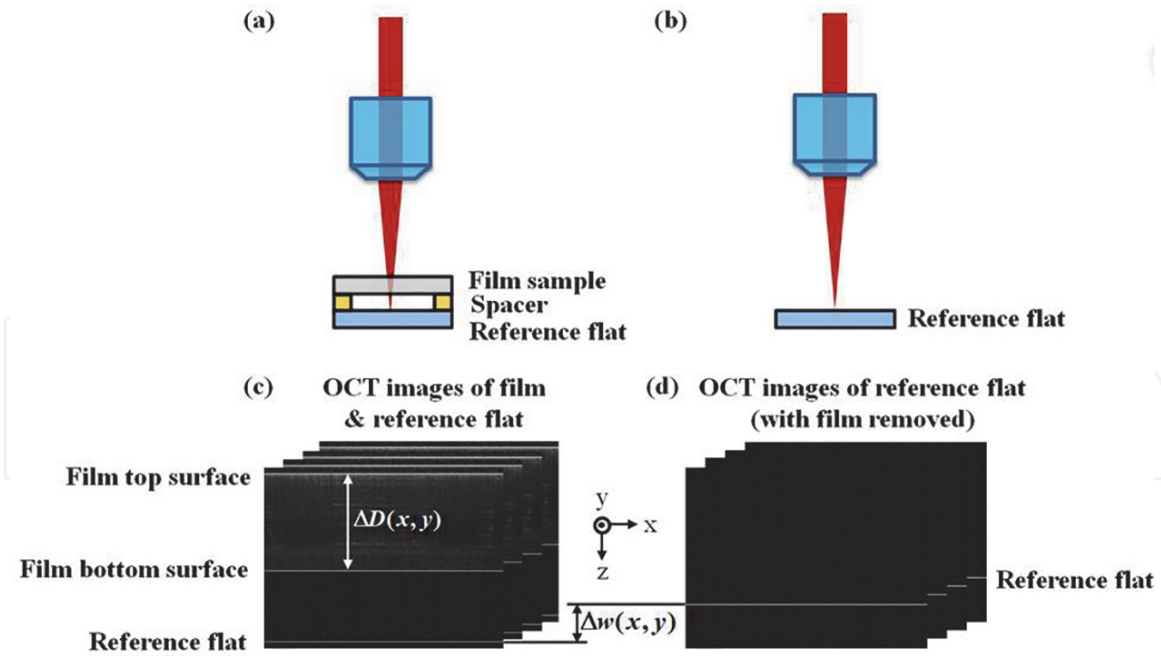


Figure 6. In the OCT sample arm, (a) a film sample and a reference flat are imaged together, and (b) the reference flat alone is imaged after the film sample has been removed. (c) and (d) are examples of cross-sectional images collected based on setup (a) and (b), respectively.

the film under test and the reference flat need to be properly aligned to ensure normal incidence of the beam on the surfaces being imaged. **Figure 6c** shows an example of raw cross-sectional OCT images collected in this setup. The optical thickness $\Delta D(x, y)$ of the film is obtained by computing the difference between the axial positions of the intensity peaks corresponding to its top and bottom surfaces, which can be expressed as

$$\Delta D(x, y) = \langle n_g(x, y) \rangle_z \cdot t(x, y). \quad (11)$$

where $\langle n_g(x, y) \rangle_z$ denotes the group refractive index averaged over the thickness of the film, and $t(x, y)$ is the physical thickness of the film, both mapped out laterally as a function of the Cartesian (x, y) coordinates. $\langle n_g(x, y) \rangle_z$ may be mathematically expressed as

$$\langle n_g(x, y) \rangle_z = \frac{\int_{z_0}^{z_1} n_g(x, y, z) dz}{t(x, y)}, \quad (12)$$

where $n_g(x, y, z)$ is the local group refractive index within the 3-D volume of a film.

Subsequently, the film sample is removed and only the reference flat was imaged again as shown in **Figure 6b**. An example of raw cross-sectional OCT images is shown in **Figure 6d**. As a result of the previous path of the film sample being replaced by air, the axial position of the reference flat on the OCT image is shifted upward by $\Delta w(x, y)$ due to its reduced optical path difference relative to the reference arm, which can be expressed as

$$\Delta w(x, y) = \left(\langle n_g(x, y) \rangle_z - n_{air} \right) \cdot t(x, y), \quad (13)$$

where n_{air} is the group refractive index of the air at the OCT operating wavelength under laboratory temperature, pressure, and humidity conditions. $\Delta w(x, y)$ reveals the change in the optical path length induced by the film sample. It can be seen from Eqs. (12) and (13) that, by measuring both the $\Delta D(x, y)$ and $\Delta w(x, y)$, the material parameters $t(x, y)$ and $\langle n_g(x, y) \rangle_z$ can be obtained simultaneously as

$$t(x, y) = \frac{\Delta D(x, y) - \Delta w(x, y)}{n_{air}}, \quad (14)$$

$$\langle n_g(x, y) \rangle_z = \frac{\Delta D(x, y)}{\Delta D(x, y) - \Delta w(x, y)} \cdot n_{air}. \quad (15)$$

$\langle n_g(x, y) \rangle_z$ and $t(x, y)$ depict the lateral refractive index distribution and physical thickness uniformity of a film sample.

4.2 Simultaneous film thickness and refractive index metrology by hybrid confocal-scan FD-OCT

By incorporating confocal-scanning-based focus tracking into an FD-OCT system, the refractive index and geometrical thickness of a film layer can be simultaneously estimated. This method is applicable to measure the refractive index and thickness of each individual layer within multi-layer film samples.

To exemplify the method, measurements on a single film sample are illustrated in **Figure 7**. By measuring the distance between the peaks of the two intensity PSFs on an FD-OCT depth profile as shown in **Figure 7b**, the group optical thickness ΔD between the top and bottom surfaces of the layer can be obtained, which is expressed as

$$\Delta D = n_g \cdot t, \quad (16)$$

where n_g is the group refractive index, and t is the physical layer thickness.

In order to extract simultaneously the group index n_g and the physical layer thickness t , an additional independent relationship between these two quantities is required. In a hybrid confocal-scan FD-OCT system, the sample arm is configured as shown in **Figure 7a**. This setup allows to obtain the additional information of the focal shift distance (Δz) needed to focus the objective lens from the top surface of the layer to the bottom surface, which yields an additional relationship between, in this case, the phase index of refraction n_p and the thickness t given as

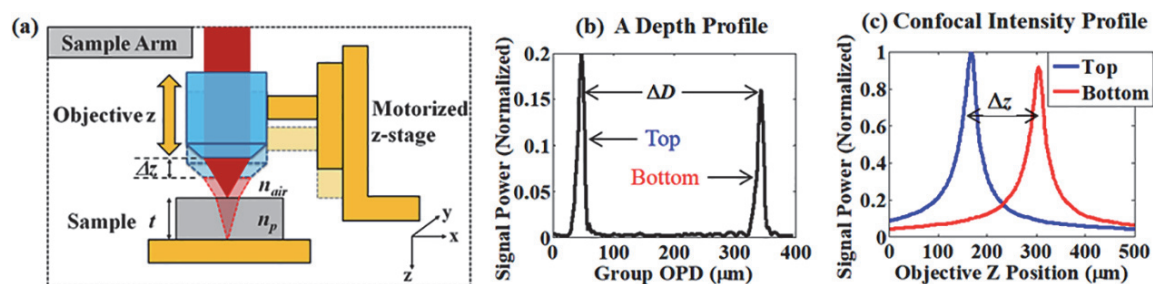


Figure 7. (a) Illustration of the sample arm of a hybrid confocal-scan FD-OCT system during measurement through a single film. (b) An example of an FD-OCT depth profile acquired when the objective is focused between the top and bottom surfaces. (c) Confocal intensity profiles of both the top and bottom surfaces reconstructed from a sequence of depth profiles acquired simultaneously with the objective lens being translated to focus through the top and bottom surfaces (adapted from [26]).

$$n_p = \sqrt{NA^2 + (n_{air}^2 - NA^2) \left(\frac{t}{\Delta z}\right)^2}, \quad (17)$$

where NA is the numerical aperture of the objective lens, and n_{air} is the phase index of the ambient air. In practice, Δz is obtained from the confocal intensity profiles of both the top and bottom surfaces as shown in **Figure 7c**, which are reconstructed in post-processing by tracing the peak amplitude of the respective PSFs on a sequence of depth profiles acquired, while the objective lens is translated to focus through the top and bottom surfaces.

Note that the refractive index involved in the confocal-scan Δz measurement is the phase index, whereas the FD-OCT ΔD measurement concerns the group index. To obtain independently the phase index, group index, and thickness of a layer, the conversion between the group and phase indices is required as described by the dispersion relation

$$n_g = n_p - \Delta n_{disp} = n_p - \lambda \frac{\partial n_p}{\partial \lambda}. \quad (18)$$

For common polymeric films, the material dispersion property, that is, $\frac{\partial n_p}{\partial \lambda}$, is assumed to be a priori knowledge that can be directly applied in Eq. (18). If the dispersion term is unknown, it can be obtained by conducting the confocal-scan FD-OCT measurements separately at another spectral band (e.g., around both 840 nm and 1300 nm). The same principle works for additional spectral bands to measure the index, thickness, and dispersion characteristic of unknown samples.

Combining Eqs. (16)–(18), n_p can be computed by solving the following quartic equation:

$$\begin{aligned} An_p^4 + Bn_p^3 + Cn_p^2 + Dn_p + E &= 0, \\ A &= (\Delta z)^2, \\ B &= -2\Delta n_{disp}(\Delta z)^2, \\ C &= [(\Delta n_{disp})^2 - (NA)^2](\Delta z)^2, \\ D &= 2\Delta n_{disp}(\Delta z)^2(NA)^2, \\ E &= -(\Delta n_{disp})^2(\Delta z)^2(NA)^2 - [n_{air}^2 - (NA)^2](\Delta D)^2. \end{aligned} \quad (19)$$

Once n_p is computed, n_g and t can be solved consecutively based on Eqs. (18) and (16).

5. Examples

5.1 3-D volumetric imaging of films

Ultra-high-resolution OCT systems, exemplified by the Gabor domain optical coherence microscopy (GD-OCM) [28, 29], enable nondestructive volumetric inspection of fine structures within otherwise transparent-appearing film samples [30].

The GD-OCM system utilizes a liquid lens embedded in a custom optical system designed to achieve dynamic focusing of the component at both axial and lateral optical resolutions of 2 μm throughout up to 2 mm. The layout of the system is detailed elsewhere [28]. The light source is a Titanium:Sapphire femtosecond laser

centered at 800 nm with 120 nm FWHM (Integral, Femtolasers Inc.). The spectral interference signal is registered onto up to 4992 pixels ($10\ \mu\text{m} \times 20\ \mu\text{m}$ per pixel) of a high-speed CMOS line camera (spl8192-70 km, Basler Inc.) through a custom spectrometer. The exposure time was set to $20\ \mu\text{s}$ and the acquisition speed was 23,000 A-lines/sec with x-y scanning by two cross-axis mirrors driven by two galvanometers synchronized to the acquisition of the CMOS camera.

In this example, two films under investigation are $50\text{-}\mu\text{m}$ thick SAN17/PMMA co-extruded polymer films, bounded by $25\text{-}\mu\text{m}$ thick protective layers on both sides. Both films, labeled as film #1 and film #2, are of the same composition, yet processed under different temperatures and pressures during fabrication. With $2\text{-}\mu\text{m}$ resolution, miniscule line and particle defects are clearly identified inside the films by the GD-OCM system. Furthermore, the locations and dimensions of the defects in 3-D are precisely measured.

Figure 8a and **b** show 3-D GD-OCM imaging of two films rendered by Voxx software (The School of Medicine, Indiana University). Film #1 exhibits more densely distributed defects compared to film #2, as shown by an ocean of particulates across the entire film volume. **Figure 8c** and **d** are two examples of enlarged *en face* (x - y plane) and corresponding cross-sectional (x - z plane) images of a few typical defects of film #2 as denoted by red arrows in **Figure 8b**. The lateral extent of the defects can be identified from the *en face* images, whereas their depth locations and extent can be accurately quantified from the cross-sectional images.

A discovery based on this metrology was that, for otherwise equivalent films, the processing temperature and pressure applied during manufacture have an important impact on the defect level in the films.

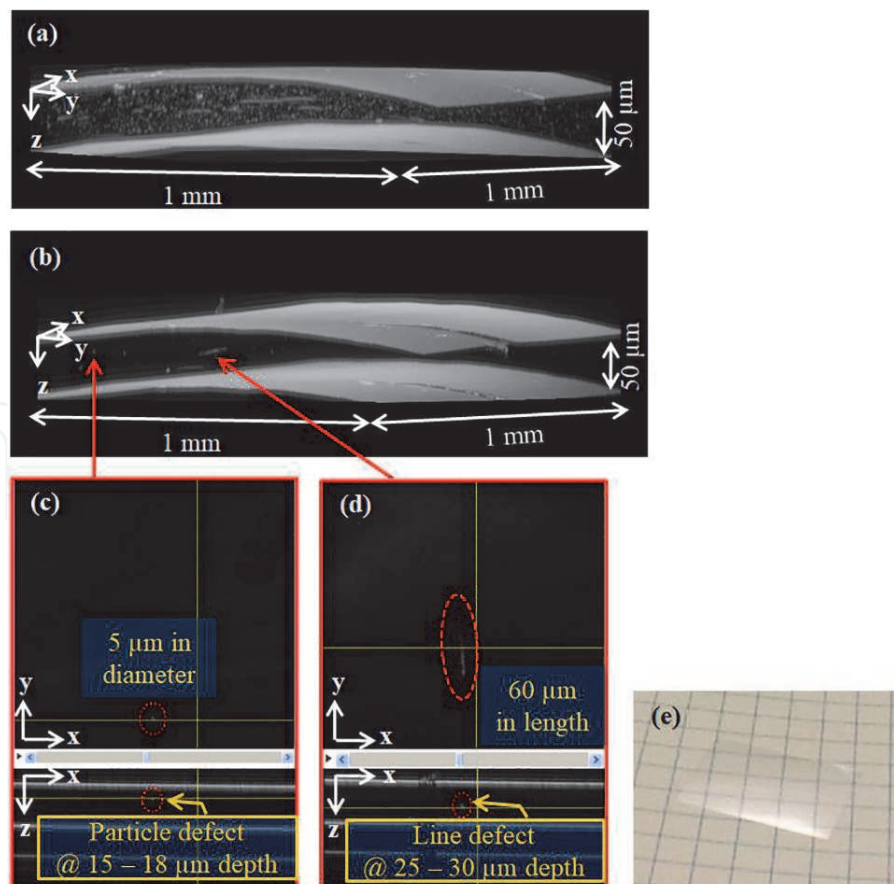


Figure 8. GD-OCM imaging of two identical composition $50\text{-}\mu\text{m}$ thick films extruded under different temperatures and pressures. (a) Film #1 showing a multitude of defects. (b) Film #2 showing few defects. (c) and (d) are two examples of enlarged *en face* and corresponding cross-sectional images of a few typical defects of film #2 in the locations denoted by red arrows in (b). (e) Photograph of a film (adapted from [30]).

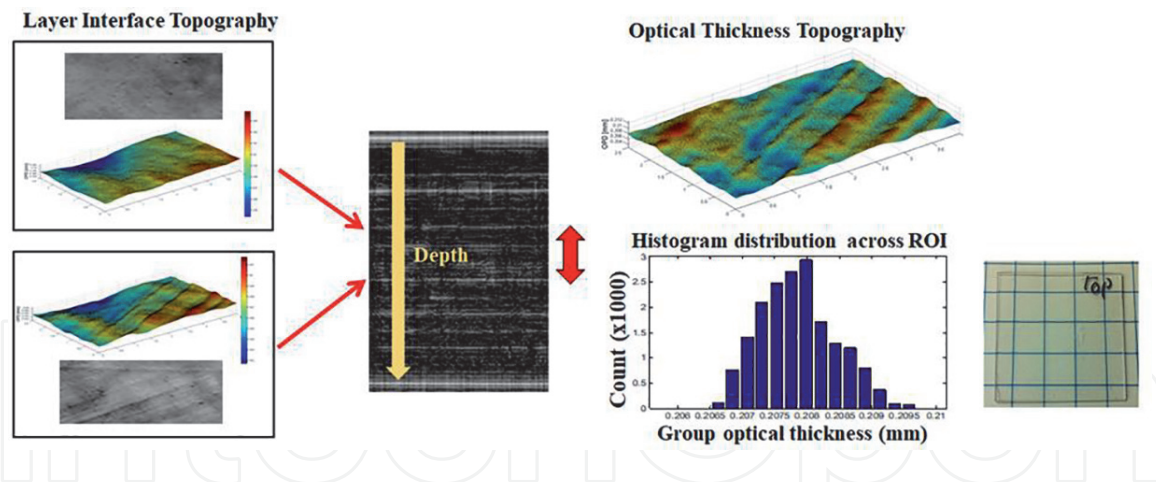


Figure 9. Illustration of film layer interfaces and optical thickness topography with statistical distribution denoted.

5.2 Film interface and thickness topography

From 3-D volumetric imaging data of film samples, accurate topography of the surfaces of a single-layer film or interfaces among a multi-layer film sample can be readily extracted by various peak detection or surface segmentation algorithms. Such topographies allow nondestructive inspection of the spatial uniformity and surface waviness of samples, which carries important value for pinpointing the locations and root causes of surface defects, particularly useful within multi-layer samples.

Figure 9 shows an example of profiling the inter-layer interfaces within a multi-layer film stack sample that visually appears transparent. The data were acquired from an SS-OCT system with an axial PSF of approximately 8 μm FWHM in air and a lateral resolution of 20 μm . The NIR light source (Micron Optics, Inc.) periodically sweeps over a wavelength range of 1240–1400 nm at a constant sweep rate of 45 kHz. The instantaneous linewidth of the source is about 0.2 nm, resulting in an imaging depth range of about 1 mm. Based on the acquired OCT imaging data, a surface segmentation algorithm is applied to produce 3-D visualization of the surface profiles of inter-layer interfaces. The difference in the topography of two interfaces leads to the optical thickness topography of film layer stack.

5.3 Metrology of film thickness through depth

As has been shown, the superb depth sectioning capability of OCT reveals not only the surfaces but also the layer interfaces within a film sample where specular or scattering reflection signals are generated from either layer-to-layer refractive index change or lamination imperfection.

A $33 \times 33 \times 2.93 \text{ mm}^3$ (x, y, z) multi-layered monolithic sheet sample was examined by an SS-OCT system with ~ 1 mm depth range as described in Section 5.2 [31]. The sample is composed of 108-layer polymer films of coextruded 10%/90% PMMA/SAN17 with nominal individual film thickness of 27 μm . Two sets of 3-D OCT data covering the top and bottom portions of the sample were collected and volumetrically rendered as shown in **Figure 10**. From the 3-D OCT data sets, a lateral location was selected where the group optical thickness of each film layer imaged by the SS-OCT system is computed and divided by the group refractive index of the sample to yield estimated geometrical thickness. **Figure 10f** and **g** are two plots of the layer thickness profiles as a function of the layer number counted from the top and the bottom surfaces of the sample, respectively, which indicate

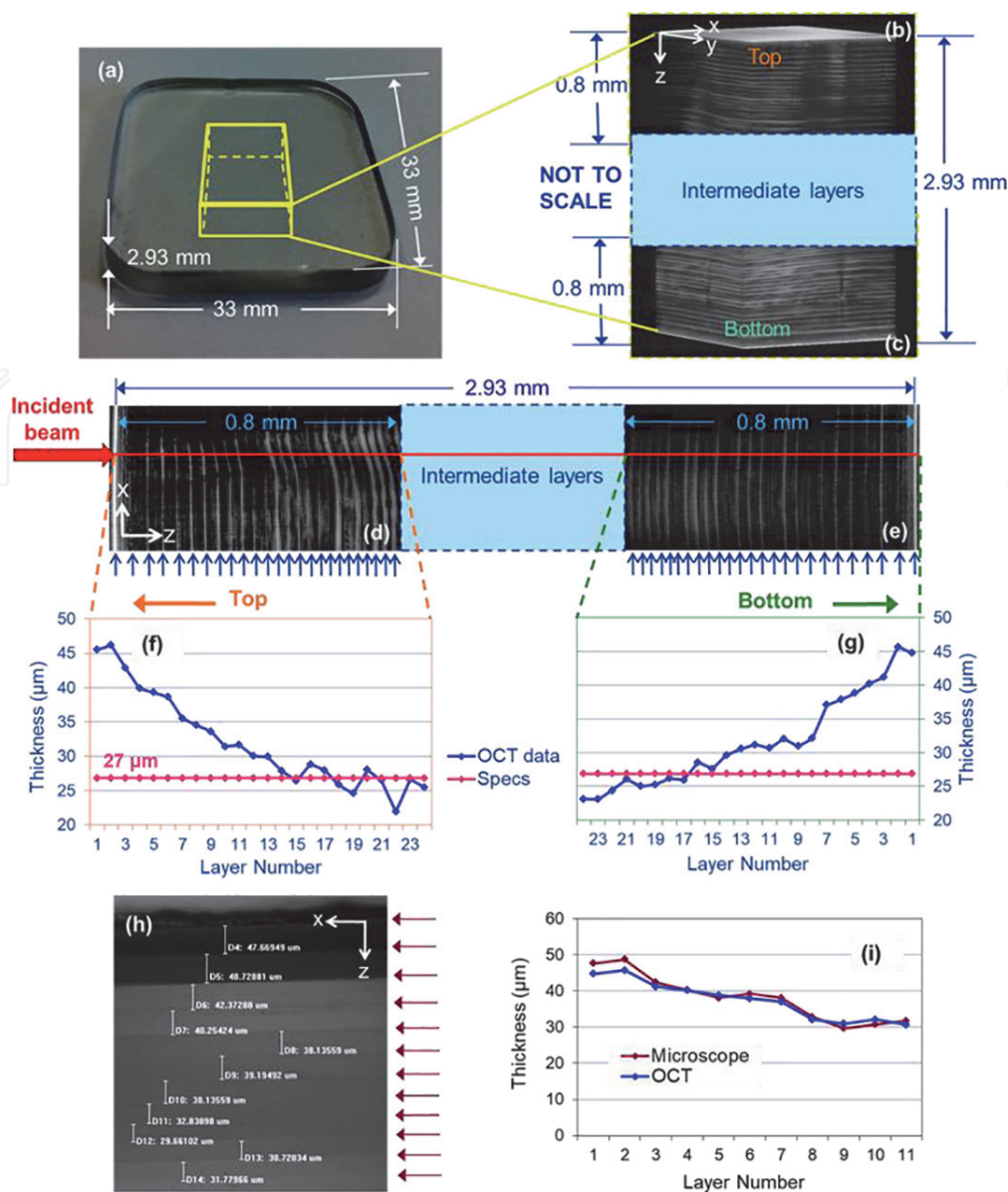


Figure 10.

Nondestructive metrology of the layer thickness profiles over the depth of a multi-layer monolithic polymeric sample. (a) A photograph of the sample. (b) and (c) are volumetric rendering of the 3-D OCT data sets of the top and bottom portions of the sample, respectively. (d) and (e) are cross-sectional OCT images of the top and bottom portions of the sample with the red line representing the location where OCT depth scans were taken for thickness estimation. (f) and (g) are layer thickness profiles of the top and bottom 23 layers, respectively. (h) A cross-sectional image of the bottom 11 layers of the sample after being cut and imaged under a light microscope. (i) Quantitative comparison of the layer thickness profiles of the bottom 11 layers obtained from OCT and microscope measurements (adapted from [31]).

that the layer thicknesses decrease from the near surface layers toward the inner layers of the sample.

The thickness measurements were confirmed by cutting the sample, polishing the cut surface, and imaging it under a light microscope with 20x magnification as shown in **Figure 10h**. From the dense layer structure imaged by the microscope, the thicknesses of the first 11 layers counting from the bottom surface were measured. The film thicknesses measured from the microscope image and those measured by SS-OCT over the same region of the sample are plotted in **Figure 10i**, which shows good agreement. The validation proves OCT as a compelling technique for nondestructive characterization of the layer thickness distribution in multi-layered polymeric material sheets despite their apparent full visual transparency.

5.4 Simultaneous refractive index and thickness metrology

Conventional OCT systems rely on a priori knowledge of the refractive index of the sample under test to estimate its geometrical thickness. Hybrid confocal-scan SS-OCT systems may provide simultaneous measurements of both the refractive index and thickness of a single- or multi-layer film sample as described in Section 4.2.

Figure 11 shows an example of the simultaneously measured refractive index and layer thickness profiles of a sample consisting of 108-layer coextruded 10%/90% PMMA/SAN17 films as described in Section 5.3. The OCT system incorporates a confocal scanning mechanism with 0.1- μm z -resolution in an SS-OCT system with ~ 5 mm depth range. The swept laser (HSL-2100-WR, Santec, Japan) is centered at 1318 nm with a FWHM spectral bandwidth of 125 nm and an instantaneous linewidth of 0.1 nm. The axial PSF of the system is approximately 10 μm FWHM in air and the effective frequency sweep rate of the source is 20 kHz.

During the confocal scan, each film surface or layer interface under test went in and out of focus, consecutively. Confocal intensity profiles were reconstructed from the entire sets of depth profiles collected to show the back-reflection intensity variations for all interfaces as a function of the axial position of the objective lens. Combining the measurements of the group optical thickness ΔD between two interfaces provided by the depth profiles and the translation Δz needed to focus from one interface to the next, the refractive index and thickness between the two interfaces were simultaneously computed. To validate the measurement consistency and uncertainty through increasing the thickness, the first surface was fixed as the top surface of the monolithic film-stack sample and the second surface was varied along depth from the first layer interface successively to the bottom surface of the sample. The measured phase refractive index and the cumulative thickness of

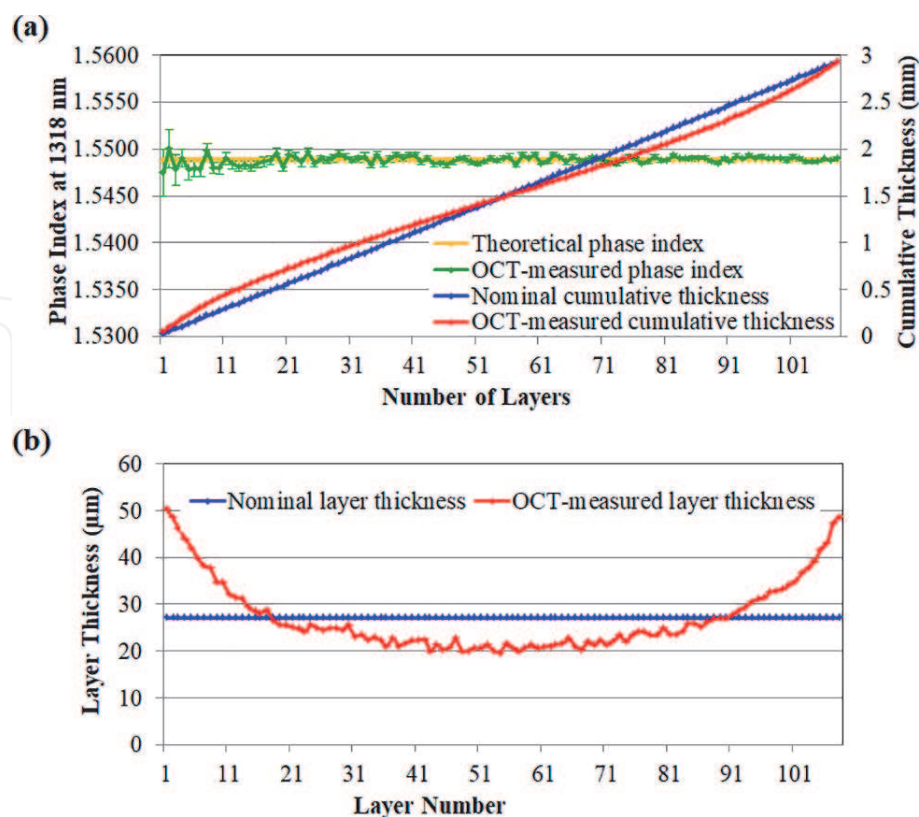


Figure 11. (a) Theoretical and OCT-measured phase refractive index and cumulative thickness of a monolithic 108-layer 10/90% PMMA/SAN17 sample measured across increasing numbers of layers. (b) Nominal and OCT-measured thickness of each layer (adapted from [26]).

1–108 layers averaged from 100 repeated measurements are plotted in **Figure 11a**, together with their standard deviations, against the theoretical values. Based on the composition of the monolith, it is predicted to have a phase index of 1.5489, while the OCT-measured index (average of 100 measurements) ranges from 1.5475 to 1.5500 and deviates from the theoretical value by about 0.00003 (measuring 106 layers, 2.8378 mm thick) to 0.0014 (measuring 1 layer, 0.0502 mm thick). The standard deviation of 100 measurements varies from 0.0001 (measuring 105 layers, 2.7946 mm thick) to 0.0025 (measuring 1 layer). It is also shown in **Figure 11a** that the measured cumulative thickness increases more rapidly near both surfaces of the sample. The standard deviation of the measured cumulative thicknesses across 100 measurements varies from 0.12 μm (measuring one layer) to 0.28 μm (measuring 105 layers).

The estimated thickness of each individual film layer was obtained by computing the difference between the cumulative thicknesses of two consecutive numbers of layers and is plotted in **Figure 11b**, which shows a nearly parabolic profile as opposed to a theoretical uniform layer thickness of $\sim 27 \mu\text{m}$. The non-uniformity in the measured film layer thicknesses helped to diagnose the issue in the fabrication process and facilitated the improvement of the process.

6. Summary and perspectives

Development of functional polymer films and film stacks has been under increasing demand to create new generations of novel, compact, light-weight optics. OCT provides the right tool for the metrology of all the key optical properties of these films, ranging from flat to curved geometries. In this chapter, the system design, metrology methodologies, and examples of OCT for film metrology are discussed to provide both the knowledge foundation and the engineering perspectives. The advanced film metrology capabilities offered by OCT, such as simultaneous refractive index and thickness estimation, and 3-D inspection of curved films by angular-scan OCT [14, 15], play a key role in the manufacturing process maturity of newly developed films. Rapid advancement in the field of OCT is foreseen to drive the application toward in-line film metrology and facilitate the rapid growth of innovative films in the industry.

Author details

Jianing Yao* and Jannick P. Rolland
The Institute of Optics, University of Rochester, Rochester, NY, USA

*Address all correspondence to: jianingyao.optics@gmail.com

IntechOpen

© 2020 The Author(s). Licensee IntechOpen. Distributed under the terms of the Creative Commons Attribution - NonCommercial 4.0 License (<https://creativecommons.org/licenses/by-nc/4.0/>), which permits use, distribution and reproduction for non-commercial purposes, provided the original is properly cited. 

References

- [1] Häusler G, Lindner MW. “Coherence Radar” and “Spectral Radar”—New tools for dermatological diagnosis. *Journal of Biomedical Optics*. 1998;**3**(1): 21-31
- [2] Wojtkowski M, Leitgeb R, Kowalczyk A, Bajraszewski T, Fercher AF. In vivo human retinal imaging by Fourier domain optical coherence tomography. *Journal of Biomedical Optics*. 2002;**7**(3):457
- [3] Nassif NA, Cense B, Park BH, Pierce MC, Yun SH, Bouma BE, et al. In vivo high-resolution video-rate spectral-domain optical coherence tomography of the human retina and optic nerve. *Optics Express*. 2004;**12**(3):367-376
- [4] Chinn SR, Swanson EA, Fujimoto JG. Optical coherence tomography using a frequency-tunable optical source. *Optics Letters*. 1997;**22**(5):340-342
- [5] Golubovic B, Bouma BE, Tearney GJ, Fujimoto JG. Optical frequency-domain reflectometry using rapid wavelength tuning of a Cr⁴⁺:forsterite laser. *Optics Letters*. 1997;**22**(22):1704-1706
- [6] Yun SH, Tearney GJ, de Boer JF, Iftimia N, Bouma BE. High-speed optical frequency-domain imaging. *Optics Express*. 2003;**11**(22):2953-2963
- [7] Huber R, Wojtkowski M, Fujimoto JG. Fourier domain mode locking (FDML): A new laser operating regime and applications for optical coherence tomography. *Optics Express*. 2006; **14**(8):3225-3237
- [8] Tearney GJ, Bouma BE, Fujimoto JG. High-speed phase- and group-delay scanning with a grating-based phase control delay line. *Optics Letters*. 1997; **22**(23):1811-1813
- [9] Iyer S, Coen S, Vanholsbeeck F. Dual-fiber stretcher as a tunable dispersion compensator for an all-fiber optical coherence tomography system. *Optics Letters*. 2009;**34**(19):2903-2905
- [10] Fercher AF, Hitzinger CK, Sticker M, Zawadzki R, Karamata B, Lasser T. Dispersion compensation for optical coherence tomography depth-scan signals by a numerical technique. *Optics Communications*. 2002;**204**(1-6):67-74
- [11] Marks DL, Oldenburg AL, Reynolds JJ, Boppart SA. Digital algorithm for dispersion correction in optical coherence tomography for homogeneous and stratified media. *Applied Optics*. 2003;**42**(2):204-217
- [12] Wojtkowski M, Srinivasan VJ, Ko TH, Fujimoto JG, Kowalczyk A, Duker JS. Ultrahigh-resolution, high-speed, Fourier domain optical coherence tomography and methods for dispersion compensation. *Optics Express*. 2004; **12**(11):2404-2422
- [13] Qi B, Himmer AP, Gordon LM, Yang XV, Dickensheets LD, Vitkin IA. Dynamic focus control in high-speed optical coherence tomography based on a microelectromechanical mirror. *Optics Communications*. 2004;**232**(1-6):123-128
- [14] Yao J, Meemon P, Ponting M, Rolland JP. Angular scan optical coherence tomography imaging and metrology of spherical gradient refractive index preforms. *Optics Express*. 2015;**23**(5):6428-6443
- [15] Yao J, Thompson KP, Ma B, Ponting M, Rolland JP. Volumetric rendering and metrology of spherical gradient refractive index lens imaged by angular scan optical coherence tomography system. *Optics Express*. 2016;**24**(17): 19388-19404
- [16] Wang D, Liang P, Samuelson S, Jia H, Ma J, Xie H. Correction of image

- distortions in endoscopic optical coherence tomography based on two-axis scanning MEMS mirrors. *Biomedical Optics Express*. 2013;**4**(10):2066-2077
- [17] Ortiz S, Siedlecki D, Remon L, Marcos S. Optical coherence tomography for quantitative surface topography. *Applied Optics*. 2009;**48**(35):6708-6715
- [18] Malacara D. *Optical Shop Testing*. 3rd ed. Hoboken, NJ: Wiley; 2007
- [19] Yao J, Anderson A, Rolland JP. Point-cloud noncontact metrology of freeform optical surfaces. *Optics Express*. 2018;**26**(8):10242-10265
- [20] Tearney GJ, Brezinski ME, Southern JF, Bouma BE, Hee MR, Fujimoto JG. Determination of the refractive index of highly scattering human tissue by optical coherence tomography. *Optics Letters*. 1995;**20**(21):2258-2260
- [21] Uhlhorn SR, Borja D, Manns F, Parel J-M. Refractive index measurement of the isolated crystalline lens using optical coherence tomography. *Vision Research*. 2008;**48**(27):2732-2738
- [22] Verma Y, Rao KD, Suresh MK, Patel HS, Gupta PK. Measurement of gradient refractive index profile of crystalline lens of fish eye in vivo using optical coherence tomography. *Applied Physics B: Lasers and Optics*. 2007;**87**(4):607-610
- [23] de Castro A, Ortiz S, Gamba E, Siedlecki D, Marcos S. Three-dimensional reconstruction of the crystalline lens gradient index distribution from OCT imaging. *Optics Express*. 2010;**18**(21):21905
- [24] Ohmi M, Ohnishi Y, Yoden K, Haruna M. In vitro simultaneous measurement of refractive index and thickness of biological tissue by the low coherence interferometry. *IEEE Transactions on Biomedical Engineering*. 2000;**47**(9):1266-1270
- [25] Kim S, Na J, Kim MJ, Lee BH. Simultaneous measurement of refractive index and thickness by combining low-coherence interferometry and confocal optics. *Optics Express*. 2008;**16**(8):5516
- [26] Yao J, Huang J, Meemon P, Ponting M, Rolland JP. Simultaneous estimation of thickness and refractive index of layered gradient refractive index optics using a hybrid confocal-scan swept-source optical coherence tomography system. *Optics Express*. 2015;**23**(23):30149-30164
- [27] Zhou Y, Chan KK, Lai T, Tang S. Characterizing refractive index and thickness of biological tissues using combined multiphoton microscopy and optical coherence tomography. *Biomedical Optics Express*. 2013;**4**(1):38-50
- [28] Lee KS, Thompson KP, Meemon P, Rolland JP. Cellular resolution optical coherence microscopy with high acquisition speed for in-vivo human skin volumetric imaging. *Optics Letters*. 2011;**36**(12):2221-2223
- [29] Canavesi C, Rolland JP. Ten years of Gabor-domain optical coherence microscopy. *Applied Sciences*. 2019;**9**(12):2019
- [30] Meemon P, Yao J, Lee KS, Thompson KP, Ponting M, Baer E, et al. Optical coherence tomography enabling non-destructive metrology of layered polymeric GRIN material. *Scientific Reports*. 2013;**3**:1709
- [31] Yao J, Meemon P, Lee KS, Rolland JP. Nondestructive metrology by optical coherence tomography empowering manufacturing iterations of layered polymeric optical materials. *Optical Engineering*. 2013;**52**(11):112111